Available online at www.sciencedirect.com

ScienceDirect

journal homepage: www.elsevier.com/locate/he

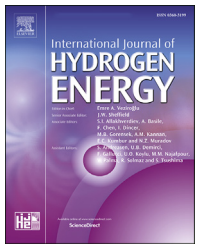

Hydrogen desorption/absorption properties of the extensively cold rolled β Ti–40Nb alloy

R.A. de Araujo-Silva [a], A.M. Jorge Jr [a,*], L.E.R. Vega [a], R.M. Leal Neto [b], D.R. Leiva [a], W.J. Botta [a]

[a] Universidade Federal de São Carlos (UFSCar), Departamento de Engenharia de Materiais, Rodovia Washington Luiz, km 235, CEP: 13565 – 905, São Carlos, SP, Brazil

[b] Instituto de Pesquisas Energéticas e Nucleares (IPEN), Av. Lineu Prestes 2242, Cidade Universitária, CEP: 05508-000, São Paulo, SP, Brazil

HIGHLIGHTS

- The stored-strain energy activates the cold-rolled β Ti–40Nb alloy for hydriding.
- Extensive cold rolling produced samples with stacked layers of the material.
- Synergistic effect of defects and layer thickness improves H-sorption properties.
- Deformation led to better absorption at RT than at 300 °C for undeformed samples.

ARTICLE INFO

Article history:
Received 20 February 2019
Received in revised form
23 May 2019
Accepted 27 May 2019
Available online 19 June 2019

Keywords:
β Ti–Nb alloy
Extensive cold rolling
Hydrogenation
Solid-state hydrogen storage

ABSTRACT

β Ti–Nb BCC alloys are potential materials for hydrogen storage in the solid state. Since these alloys present exceptional formability, they can be processed by extensive cold rolling (ECR), which can improve hydrogen sorption properties. This work investigated the effects of ECR accomplished under an inert atmosphere on H_2 sorption properties of the arc melted and rapidly solidified β Ti40Nb alloy. Samples were crushed in a rolling mill producing slightly deformed pieces within the millimeter range size, which were processed by ECR with 40 or 80 passes. Part of undeformed fragments was used for comparison purposes. All samples were characterized by scanning electron microscopy, x-ray diffractometry, energy-dispersive spectroscopy, hydrogen volumetry, and differential scanning calorimetry. After ECR, samples deformed with 40 passes were formed by thick sheets, while several thin layers composed the specimens after 80 passages. Furthermore, deformation of β Ti–40Nb alloys synthesized samples containing a high density of crystalline defects, cracks, and stored strain energy that increased with the deformation amount and proportionally helped to overcome the diffusion's control mechanisms, thus improving kinetic behaviors at low temperature. Such an improvement was also correlated to the synergetic effect of resulting features after deformation and thickness of stacked layers in the different deformation conditions. At the room temperature, samples deformed with 80 passes absorbed ~2.0 wt% of H_2 after 15 min, while samples deformed with 40 passes absorbed ~1.8 wt% during 2 h, excellent results if compared with undeformed samples hydrogenated at 300 °C that acquired a capacity of ~1.7 wt% after 2 h. The hydrogen desorption evolved in the same way as for absorption regarding the deformation amount, which also influenced desorption temperatures that were reduced from ~270 °C, observed

* *Corresponding author.*
E-mail addresses: moreira@ufscar.br, Jorge.Moreira@lepmi.grenoble-inp.fr (A.M. Jorge Jr).
https://doi.org/10.1016/j.ijhydene.2019.05.211

for the undeformed and samples deformed with 40 passes, to ~220 °C, for specimens rolled with 80 passes. No significant loss in hydrogen capacity was observed in the cold rolled samples.

Introduction

Besides being a renewable energy resource and economically sustainable, hydrogen is also recognized as a clean energy vector, which does not emit any toxically gases [1–3]. Because the high effectiveness of hydrogen in generating power, apart from its traditional uses in the oil industry and the synthesis of ammonia and methanol, it could be employed as fuel for power generators such as fuel cells and electric vehicles, having the as significant advantage the generation of water as the only by-product [4,5].

However, the use of hydrogen as energy vector must envisage the implementation of a storage method that is simple, safe and economically viable, allowing the widespread employment of H_2 as the future energy carrier [6]. Conventional means of hydrogen storage comprised liquid hydrogen and high-pressure gas cylinders. Technological challenges restrict such kinds of storage; respectively, the temperatures at the cryogenic level and advanced high-pressure containers for the highly compressed hydrogen gas, and in both cases, the large weights and sizes [7].

For the sake of solving the hydrogen storage issue, among others in the current literature [8–14], the use of metal hydrides as solid-state hydrogen storage media is an interesting perspective to overwhelm the mentioned shortcomings of gassy and liquid options [15,16]. Among reversible hydrides to store hydrogen, alloys with BCC structure such as β-Ti-based alloys, which are traditionally used in biomedical and other functional applications [17–31], are also being considered as likely materials for hydrogen storage [32–40].

Furthermore, numerous investigations in such types of alloys have been performed considering phase transformation under hydrogen atmosphere [41,42], hydrogen permeability [43–45], hydrogen diffusion [46,47] and hydrogen influence on plastic deformation behavior [48].

The β-Ti-based alloys can be produced by alloying the transition metals Ti and Nb. Ti–Nb equilibrium phase diagram exhibits two solid phases: α and β. The α-phase has a hexagonal crystal structure (hP2), and pure Ti has an allotropic phase transformation at about 890 °C changing to a body-centered cubic crystal structure (BCC), or β-phase (cI2) [49]. Nb addition lowers the α → β transformation temperature being a stronger β stabilizer, having the same effect as other transition metals such as Mo and V. In Ti–Nb alloys the β-phase, which is a solid solution with extensive solid solubility, can be stable until room temperature. Besides these two stable phases, the Ti–Nb system exhibits non-equilibrium phases such as hexagonal martensite (α'), orthorhombic martensite (α") and hexagonal ω phase [19,50,51].

The BCC alloys of the Ti–Nb system produces hydrides with a face-centered cubic structure (FCC) [33,37]. The Nb content influences their hydrogen capacities and desorption temperatures. The increase of Nb content in the alloy leads to a reduction in hydrogen storage capacity and a decrease in the desorption temperature [33,52]. Furthermore, the hydrogen storage at niobium containing sites results in a higher diffusion coefficient due to the lower activation energy for hydrogen diffusion on these sites [47], assisting in improvements of hydriding kinetics.

Both Ti and Nb are hydride formers. However, Ti hydrides or Nb hydrides have large negative enthalpies of formation [53], which are responsible for the main drawback of such single metal hydrides with desorption temperatures above 500 °C for TiH_2 and in the range of 120 °C–480 °C for NbH_2 and NbH [33]. Appreciably reduced enthalpies of formation can be obtained from alloys and intermetallic compounds when compared with single metal hydrides, and for example, the Ti–Nb hydrides reach desorption temperatures between those for NbH_2 and TiH_2 [33], indicating that Nb diminishes the enthalpies for the Ti–Nb hydride formation, thus decreasing the bond strength of metal-hydrogen as compared to Ti–H system.

In addition to the choice of alloy composition, another challenging aspect is the choice of the correct route for processing metallic hydride formers to optimize their hydrogenation properties. Several distinct processing routes to produce Ti–Nb alloys are described in the literature [17,18,23,33,37,54,55]. Amid these routes, one of the most used is the high-energy ball milling (HEBM), which is a solid-state process that can synthesize such alloys from their elemental powders. The reduction of crystallite sizes to the nanosize range and refinement of particles induced by ball milling techniques improves the kinetics of H-absorption and desorption [15]; even if particles are agglomerated, they are retained in the nanoscale range. Smaller crystallite sizes will lead to a vast increase of interfaces, and the specific surface area is increased by the reduction of particle sizes, both leading to a positive effect on the H-absorption/desorption kinetics.

The beneficial effects of Nb on the microstructural features of β-Ti-Nb-based BCC solid solution alloys led to a positive influence on the kinetic behavior and desorption temperatures [36,52]. However, the decreased thermodynamic stability of formed hydrides is one of the challenges that hinder the application of these alloys as hydrogen storage material, as it was shown in recent studies [33,52] that reported high H-desorption temperatures for such alloys. However, beneficial effects of the Nb associated to HEBM on the decreasing H-desorption temperatures and novel techniques such as plasma milling and magnetron sputtering have been shown to

improve the dehydriding kinetics and the thermodynamic behaviors of hydrides [56–62].

In our previous work [52], we have reported the production of different compositions with Ti/Nb atomic ratios of 1.0, 1.5 and 2.3 by mechanical alloying (MA) and reactive milling (RM), and the composition effects on the microstructure and the hydrogenation properties were characterized. The results demonstrated a significant influence of Ti/Nb atomic ratios on lattice parameters, crystallite and particle sizes, effective kinetic parameter, hydrogen storage capacities, reversibility, and desorption temperature ranges. The hydrides synthesized by RM acquired better H-absorption/desorption properties than the ones produced by MA.

Nonetheless, ball milling is invariably a challenge. The contamination by oxygen during ball milling, even in an argon atmosphere, results in a notable decrease in the hydrogen capacity [34]. Such contamination leads to the formation of TiO_2 oxide on the sample surface that reduces the hydrogen permeation, which is critical for the H absorption kinetics [63]. Furthermore, other drawbacks are the long processing time, the potential fire risk due to powder reactivity and health concerns.

To surpass these various deficiencies and in an attempt to improve the hydrogenation properties at room temperature of the Ti–40Nb alloy, we have used in the present work a new route combining rapid solidification in water-cooled copper crucible followed by cold rolling. Arc-melted Ti–Nb alloys exhibit a complex array of fine columnar dendrites with the possibility of Nb microsegregation [64]. Fast cooling can lead to very fine grain sizes, which can be further refined by additional cold rolling [19]. It is also reported that cold rolling deformation has a beneficial effect on the hydrogen storage capacity [36]. The use of such combined processing is justified by the refinement of grains and particles and the introduction of cracks that may favor the hydrogen absorption due to the increase in the specific surface area [15].

Experimental

The raw materials used in this work were powders of Ti (<45 μm and 99.98% purity) and Nb (<45 μm and 99.8% purity), both from Sigma-Aldrich.

The powders were weighted according to the atomic ratio (Ti/Nb) of 1.5 and then mixed in the Fritsch Pulverisette 6 planetary mill. The mixture was carried out under an argon atmosphere with no milling balls for 1 h at 400 rpm. The resulting mixture was first compacted by hand under purified argon using a die with 16.2 mm diameter, followed by a hydraulic pressing at a maximum pressure of 2 tons under air.

Compacted samples were evacuated to 10^{-2} mbar and then arc-melted under 1000 mbar of argon, in an Arc Melting D72379 Edmund Bühler GmbH. After four operations of remelting to assure chemical homogeneity, the resultant ingot was rapidly solidified in a water-cooled copper crucible. Such ingot was then crushed in a rolling mill producing slightly deformed particles. Part of this particulate was cold rolled with 40 passes (CR40) and 80 passes (CR80) at 40 Hz inside an MBRAUN glove box under high-purity argon atmosphere. The oxygen and moisture levels were below 0.1 ppm. To compare the hydrogen absorption properties in samples processed by different routes, part of the as-crushed material was kept without further processing.

The morphological, microstructural, and chemical characterizations were performed by scanning electron microscopy (SEM), using an FEI Inspect S-50 microscope equipped with energy-dispersive spectroscopy (EDX) system (EDAX-AMETEK). Chemical microanalyses were carried out on five random regions of the matrix (dendrite and interdendritic arms) of the as-cast material.

X-ray diffraction (XRD) analyses were performed in a Siemens D 5005 diffractometer using CuKα radiation ($\lambda = 1.5418$ Å). The samples were scanned using the 2θ range of 5–90° with an angular step of 0.032°, and a time/step of 1 s.

Crystallite sizes, microstrain values, and the fraction of phases were evaluated only for mechanically processed samples, through the Rietveld refinement using the Maud software [65,66]. Refinement of XRD spectra for hydrogenated samples was not performed because of CIF files that could fit the spectra of the FCC hydride were not found in the literature. Indeed, the literature reported the $Ti_{0.6}Nb_{0.4}H_{1.9}$ FCC hydride [33]. However, the CIF file for such phase was not published.

Here it could be interesting to remember that the only phases present in the Ti–Nb system are either cubic, hexagonal, trigonal (ω, which can also be hexagonal) or orthorhombic (α" martensite). Except for the orthorhombic martensite, no other phase produces Bragg's reflections close to peaks observed in the XRD patterns of non-hydrogenated samples. All CIF files for orthorhombic martensite belong to the space group Cmcm, which produces peaks closer to the ones seen in such XRD patterns. However, none of such CIF files for the orthorhombic phase could exactly fit any of our spectra. By observing peak positions for such martensite in our previous work [52], it was noticed that they have a strong CFC character, which is not feasible for the Ti–Nb system. The observation that EDX analyses for dendrites resulted in ~20 at % of Nb allowed estimating an atomic occupancy.

Furthermore, this amount of Nb can confirm the presence of the orthorhombic-α" phase because it favors its formation [19,49–51]. Therefore, the CIF file ICSD 166690, which presents almost the same occupancy and produces Bragg peaks closer to the ones of the XRD spectra, was modified using the software VESTA (http://jp-minerals.org/vesta/en/) to simulate parameters that could represent the phase.

Finally, simulations indicated the Fmm2 space group, giving a face-centered orthorhombic structure. The resulting peaks' positions of such simulation can be seen in Figure S1 (supplementary file).

For the refinement of the cubic β phase, it was used the CIF file ICSD 645545 that was also decided according to EDX analyses that gave the value of ~50 at% of Nb for the matrix, indicating the occupancy and directing us to such ICSD file.

Hydrogen absorption kinetic curves were obtained using a home-made Sievert-type apparatus. The purity of the H_2 gas is 99.998%. Measurements started with an initial pressure of 2 MPa. Parameters related to the kinetic experiments are detailed in Table 1.

For calculation the percentage by weight of H_2, the following procedure was used. Considering the hydrogen as an ideal gas, the Volumetric Method was applied to obtain H_2 wt% using the equations suggested by Varin et al. [15]:

Table 1 – Parameters used to determine the hydrogen absorption kinetics.

Samples	Temperature	Time
As-crushed sample	300 °C	15 h
Sample CR40	RT (~25 °C)	2 h
Sample CR80	RT (~25 °C)	15 min

$$\text{wt. \% } H_2 = (m_H \times 100)/(m_{Hydride}) \quad (1)$$

$$m_H = \left(2.016 \times \Delta P \times V/(R \times T)\right) \quad (2)$$

$$m_{Hydride} = m_H + m_s \quad (3)$$

Where wt.% H_2 is weight percent of molecular hydrogen, m_H is the molecular mass of absorbed hydrogen calculated using the number of gas moles $\left(\Delta n = \left(\Delta P \times V/(R \times T)\right)\right)$, and m_s is the metal mass (mass of Ti–Nb alloy). Thus $m_H + m_s$ is the hydride mass. To calculate the molecular mass, R is universal gas constant ($R = 8.314472\ J\ mol^{-1}\ K^{-1}$), V_h is the calibrated volume of the holder at the furnace temperature, $V = V_h + V_r$, V_r is the calibrated volume at the reservoir temperature. T (K) represents either T_f (H-absorption temperature inside of the furnace) or T_r (the room temperature), and $\triangle P$ is the range of pressure of hydrogen gas in the system during hydrogen absorption.

Differential scanning calorimetry (DSC) measurements characterized the thermal stability of the phases in the Ti–40Nb alloy and the hydrogen desorption temperatures, while thermogravimetric analyses (TGA) simultaneously measured the hydrides' gravimetric capacities. All thermal analyses were performed in the NETZSCH STA-449C equipment using 10 mg of hydrogenated samples at a heating rate of 10 K/min under an argon flow of 25 ml/min.

Results and discussions

Characterization of the samples

Fig. 1 presents secondary electrons (SE) SEM images showing typical morphological aspects of the as-cast sample (a), as-crushed sample (b), and the cold rolled samples, CR40 in (c) and CR80 in (d). Fig. 1a shows that the solidification mode was dendritic. The inset of Fig. 1a presents a chemical composition

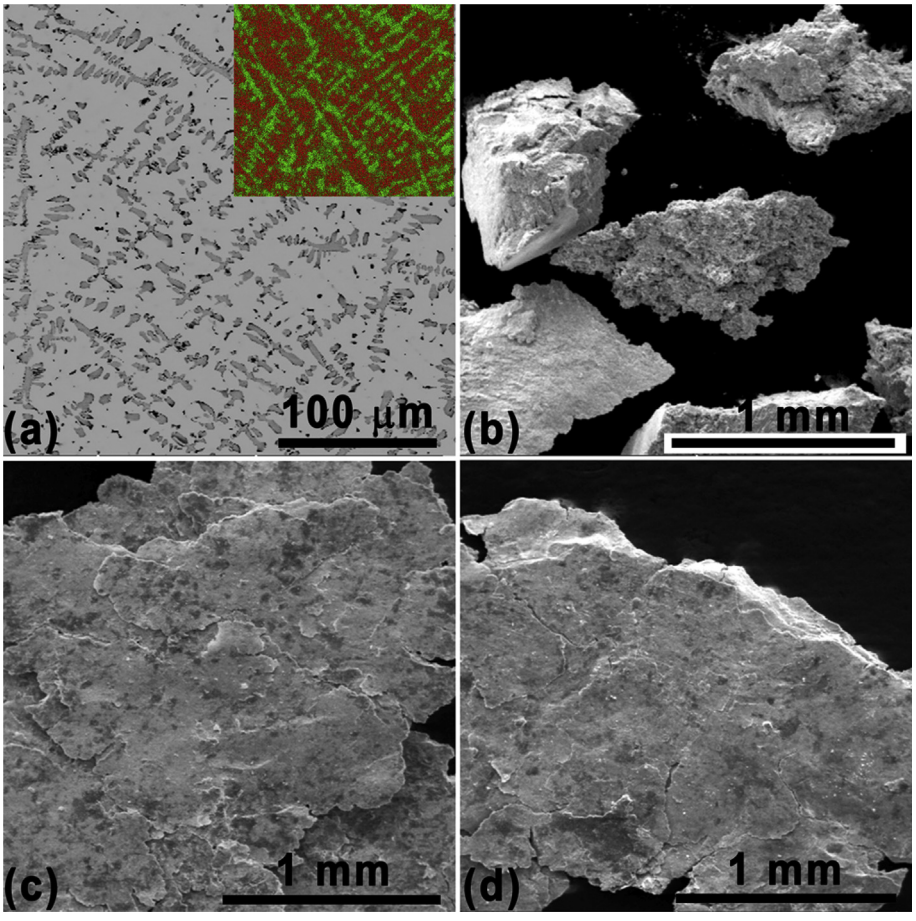

Fig. 1 – SE-SEM images. (a) as-cast sample showing the formation of dendrites. The inset shows the chemical composition map of a region of the sample, where the green color (dendrites) represents Ti, and the red one represents Nb. (b) As-crushed particles, (c) sample after 40 cold rolling passes, (d) sample after 80 cold rolling passes. (For interpretation of the references to colour in this figure legend, the reader is referred to the Web version of this article).

map acquired by the EDX system, where the green color (dendritic arms) represents a Ti richer composition and the red color (interdendritic region) an Nb richer composition. EDX analyses revealed that the matrix (interdendritic region) is composed of ~50 at% of Nb, while within dendrites the amount of Nb is ~20 at%.

From Fig. 1b, it can be observed that the as-crushed sample presents irregular coarse and thick particles. Measurements indicate that most of these particulates have about 0.8 mm in length and 0.6 mm in width, with an average thickness of about 0.8 mm.

Cold rolling of crushed particles (Fig. 1c and d) have broken and redistributed dendrite arms (darker regions in the figures) and also resulted in the formation of plate-like particles composed by overlapped layers of foils, probably the result of the stacking of several deformed particles over each other. Also, measurements gave an average value of 4 mm for particles' surface size for sample CR40 and 3 mm for sample CR80.

Fig. 2 presents the details of particulates shown in Fig. 1c and d. As one may observe, the foils are cracked, stacked, and not entirely bonded like a "puff pastry." Evaluation of the thickness of such foils indicates that it is not uniform in the sample CR40 (Fig. 2c), which is composed by few foils of around 2 μm thick on the surface (Fig. 2c upper) and 25 μm thick at the center (Fig. 2c lower) with much fewer layers than in the sample CR80 where thicknesses of foils are homogeneous and are about 2 μm thick (Fig. 2d). These features may be necessary for the hydrogenation properties since the surface area of the samples will be the result of a high number of very thin stacked foils in the sample CR80 when compared with thicker and fewer foils forming sample CR40. Furthermore, reports in the literature [67–70] mention the influence of sample thickness in the hydrogenation properties, suggesting that the thinner the samples, the better the properties.

Fig. 3a presents XRD patterns with the structural evolution of the mechanically processed samples. The indexation of Bragg peaks of such XRD patterns revealed the presence of the phases BCC-β and the orthorhombic-α". In the methodology topic, a description was given how the α" was identified, and the Rietveld refinement was performed. However, it is worthy to emphasize here that the only phase whose Bragg reflections were close to the observed peaks in the patterns of Fig. 3 was the α". No other possible phase for the system Ti–Nb had the same characteristics.

Furthermore, according to the EDX analyses, dendritic regions (Fig. 1) of the as-cast ingot presented ~20 at% of Nb, which may favor the formation of the orthorhombic-α" phase [19,49–51].

Additionally, there are reports where similar XRD patterns to the ones of this work that shows the presence of the orthorhombic-α" in Ti–Nb based alloys [71,72].

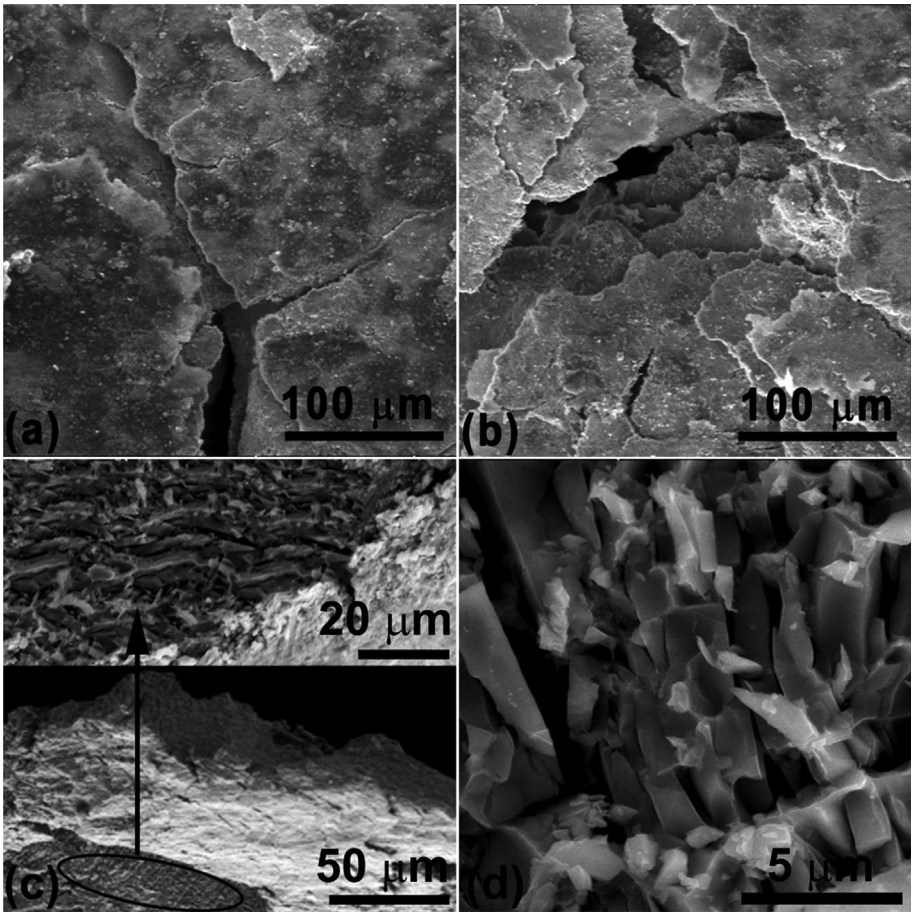

Fig. 2 – SE-SEM images presenting details of samples deformed with 40 (a and c) and 80 (b and d) cold rolling passes.

Table 2 – Fraction of phases (%) present in the mechanically processed samples, the crystallite size (D) and microstrains (e) of the β-phase after mechanical processing. Data obtained from the XRD patterns after Rietveld refinement.

Sample	Fraction of phases (%)		D (nm)	e (%)	Gof[a]
	Phase				
	α" (orthorhombic)	β (BCC)	β (BCC)		
As-crushed	21	79	24	0.4	1.35
As-rolled (CR40)	23	77	19	0.7	1.2
As-rolled (CR80)	23	77	11	0.9	1.15

[a] Gof = *Goodness of fitting (Gof = Rw/Rexp), satisfactory ≤ 1.3.

Moreover, besides the composition range, high cooling rates, as the one used in this work, were reported [71] as being one of the processing parameters responsible for allowing martensitic α" transformation, while slow cooling facilitates the direct conversion of the β to the α phase. As stated before, confirming the observed in the literature, possible Bragg's peaks for α-phase are far from the ones found in the patterns of Fig. 3a, clearly suggesting the presence of α" phase.

Table 2 displays data obtained from the XRD patterns of Fig. 3a after Rietveld refinement: the fraction of phases present in the mechanically processed samples, and crystallite size (D) and microstrains (e) of the β-phase, which are the most important for this study. A complete set of results from Rietveld refinement, including Rietveld refined XRD patterns, are presented in the supplementary material (Figs. S2–S4 and Tables S1–S5). As one may observe in such Figures and Tables, except crystallite size and microstrains, all other parameters, as expected, were kept almost constant, small differences may be related to refinements. Regarding Table 2, only a slight increase in the martensite fraction was observed with increased deformation, which is a positive aspect of cold rolling since the presence of α" phase is deleterious for the hydrogen storage capacity [52]. This behavior can also be clearly observed in the XRD results of Fig. 4, whose patterns suggest that, unlike β-Ti, the α" phase did not transform into a hydride at the evaluated hydrogenation conditions used in this work.

Another feature that can be observed in Fig. 3a is the presence of texture along the (200) and (211) crystalline planes, which was developed during ECR processing.

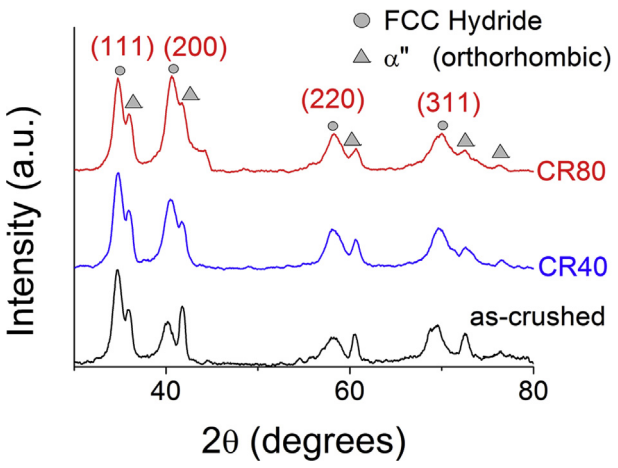

Fig. 4 – XRD patterns showing results for as-crushed sample hydrogenated at 300 °C for 15 h, sample CR40 hydrogenated at RT for 2 h, and CR80 hydrogenated at RT for 15 min.

However, the acquired textures are similar for CR40 and CR80 samples. Rietveld refinement, presented in Table 2, revealed that after fast cooling, the crystallite size of the β-phase was about 24 nm. After ECR processing, such refinement indicated that the crystallite sizes reduced to 19 nm for sample CR40 and 11 nm for sample CR80. Also, lattice strains are presented in Table 2, which shows that they were 0.4%, 0.7%, and 0.9% respectively for samples as-crushed, CR40, and CR80.

Fig. 3b presents DSC analyses of the samples Ti40Nb alloy for different mechanical processing conditions. DSC curves exhibit a massive change in enthalpy within the range of temperatures of 100–700 °C before the martensitic transformation peak, denoting that stress relief and recrystallization are taking place. In other words, such significant enthalpy change represents a massive elimination of stored energy in the form of dislocations and subgrain boundaries, even grain boundaries by recrystallization, which are the predominant defects in the mechanically processed sample, and leading, finally, to grain growth. The inset of Fig. 3b summarizes the values of stored energy for the three mechanically processed samples obtained by DSC tests. The stored energy increases with the amount of deformation from 27.6 to 35.4 kJ/mol, and peak temperatures decrease for higher deformation amounts.

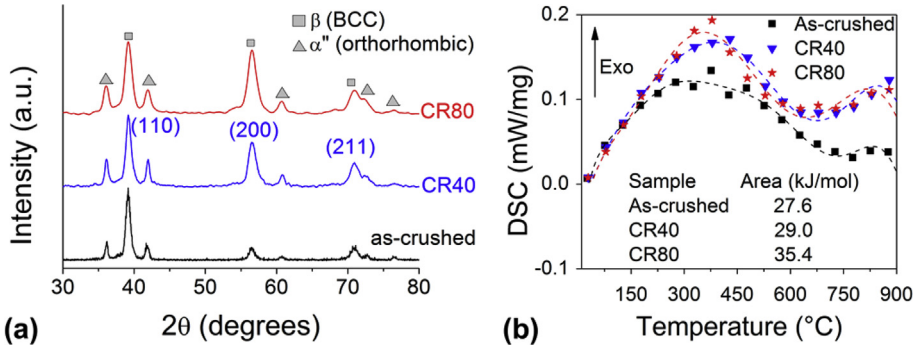

Fig. 3 – (a) XRD patterns showing the structural evolution of mechanically processed samples. (b) DSC analysis of the samples Ti40Nb alloy for the different mechanical processing condition.

The approximate value of the absorption activation energy for these samples, without the influence of ECR, was calculated using milled powders of the same composition, that were previously heated under vacuum in the Sieverts apparatus to eliminate any effect of deformation. In this way, the apparent activation energy for absorption was calculated using the Arrhenius-type equation:

$$ln(t_{0.5}) = -\left(\frac{E}{k_B T}\right) + A$$

where $t_{0.5}$ is the time for 50% of transformation, E is the activation energy, k_B is the Boltzmann constant, T is the absolute temperature, and A is a constant. The slope of the straight line of the plot ln (t0.5) vs. (1/T) gave the value for the activation energy. The used temperature range was between 25 °C and 300 °C.

Finally, the resulting value was about 119 ± 6 kJ/mol. Unfortunately, data for comparison are not available in the literature for this composition and even in this range of temperature. However, as one may observe, the stored energy, presented in the graph of Fig. 3b, may contribute significantly to a decrease in the apparent activation energy. Such a reduction is inside the range of 23–30%, values considerably high.

Characterization of hydrides and hydrogenation properties

Fig. 4 presents the XRD patterns of hydrogenated samples. Here it is important to remember that, as shown in Table 1, the as-crushed sample was hydrogenated at 300 °C for 15 h, sample CR40 at RT for 2 h, and sample CR80 also at RT, but for only 15 min. As it can be observed in Fig. 4, the BCC β phase (Fig. 3) was transformed into an FCC hydride after hydrogenation of mechanically processed samples. Within the above conditions, one can see that the hydrogenation process was not completed even after 15 h in the case of the as-crushed sample. As observed in our previous work [52], the incomplete hydrogenation is due to the presence of α"-Ti phase. These values can be compared with the Ti–Nb hydride, $Ti_{0.6}Nb_{0.4}H_{1.9}$ reported in the literature [33], whose hydrogen storage capacity is 2.87 wt% and desorption temperature at 360 °C.

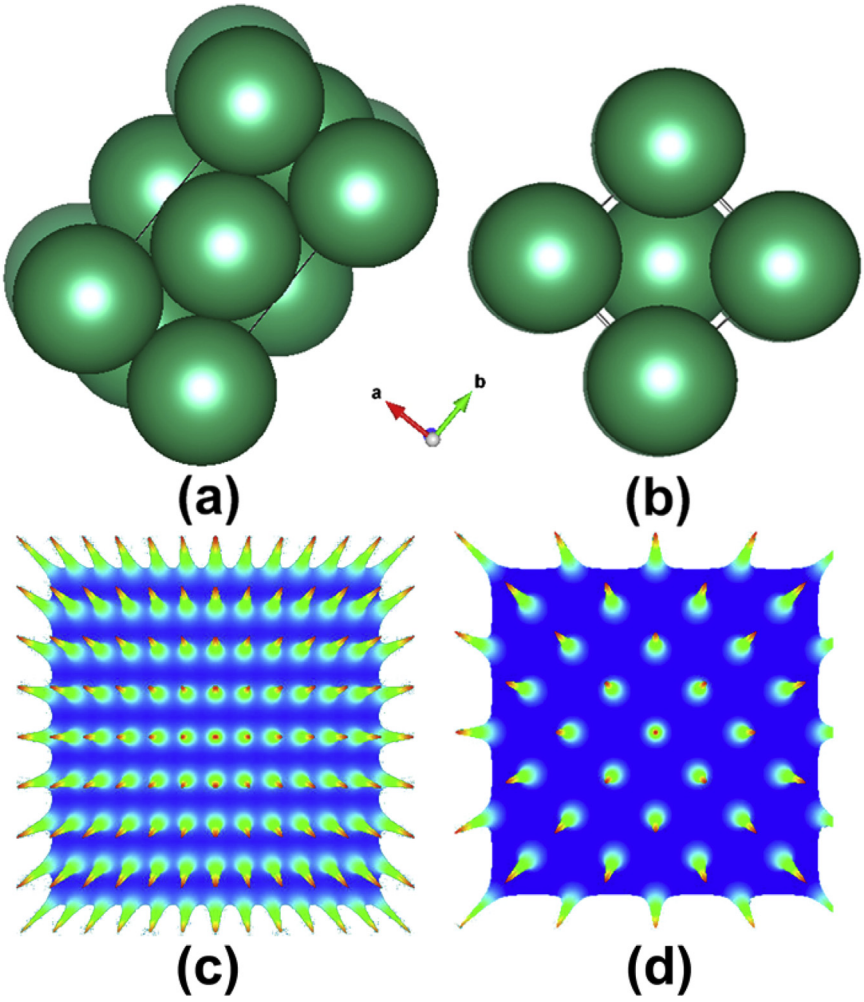

Fig. 5 – Comparison of the final structure of the orthorhombic phase after simulation in (a), compared to the cubic one in (b). Simulation of high-resolution electron transmission microscopy of the density distributions of the projected potential taking into account the variations in the z-direction on the frozen (001) surfaces, respectively for the α" phase and the β-matrix.

It could be interesting discussing the reason why the α"-Ti phase could not be hydrogenated, as it was not done before in our previous work [52]. Such lack of hydrogenation may be related to packing efficiency and number of possible tetrahedral and octahedral sites for hydrogen penetration. Fig. 5 compares the final structure of the orthorhombic phase after simulation (Fig. 5a) compared to the cubic one (Fig. 5b). As one may observe, the orthorhombic phase is much more compact than the cubic. Indeed, calculations gave the values for the packing efficiency of ~78% and ~68%, respectively for the α" and β. Furthermore, irrespectively the size of void sites, the BCC phase has 12 tetrahedral and six octahedral sites per unit cell (a total of 18 void sites), while the orthorhombic phase has only eight tetrahedral sites and four octahedral sites (a total of 12 sites). In other words, in a competition between α" and β, it will be easier for the hydrogen penetration in the last than in the former.

For the sake of confirming such a hypothesis, JEMS software [73] was employed to simulate high-resolution transmission electron microscopy (HRTEM) of the Density Distribution of the Projected Potential (DDPP) taking account of variations in the z-direction on the frozen [001] surfaces. Fig. 5c and d present the results of such simulations, respectively for the α" and β phases. The reaction with hydrogen on the surface of the sample is kinetically hampered due to its relatively weak ability to dissociate H2 or to the formation of a stable surface which limits the diffusion of atomic hydrogen into the matrix. From these simulations, one may observe that the highest degree of minimal energy positions are found for the cubic phase, and the lowest extent is found for orthorhombic one. The local minima in Fig. 5d, corresponding to the blue color, are more noticeable, and these sites can be a stable surface for hydriding. Such stability improves the rate-limiting dissociation of the hydrogen molecules on the sample surface and diminishes the limit for hydrogen atomic diffusion into the β-matrix, which is not the case for the α" phase.

Fig. 6a present kinetic measurements of the first absorption for the mechanically processed samples hydrogenated with the conditions indicated in Table 1. To better visualization and comparison, the curves are plotted only up to 140 min (2.33 h). For complete information regarding final capacities, please refer to Table 3 that summarizes the hydrogen absorption capacities for all the samples.

Absorption results indicate that the increase of deformation accelerates hydrogenation rates, even comparing with the as-crushed sample that was hydrogenated at 300 °C (Fig. 6a). Also, one may anticipate that the hydrogenation reaction ends faster in more deformed samples. The H-absorption kinetics for samples hydrogenated at RT and 300 °C and the ranging of absorption rates indicates faster kinetics as the deformation increases.

In general, faster kinetics are attained for samples deformed by cold rolling, increasing with the number of CR passes. If one pay attention in Fig. 2 (please see related discussion), as earlier reported [67–70], faster kinetics could be readily correlated with the different sample thicknesses. The cooperative effect of the stacking of very fine foils (~2 μm) with a very high surface area in sample CR80 will allow the full hydrogenation of partial thin bulk layers rapidly. However, in

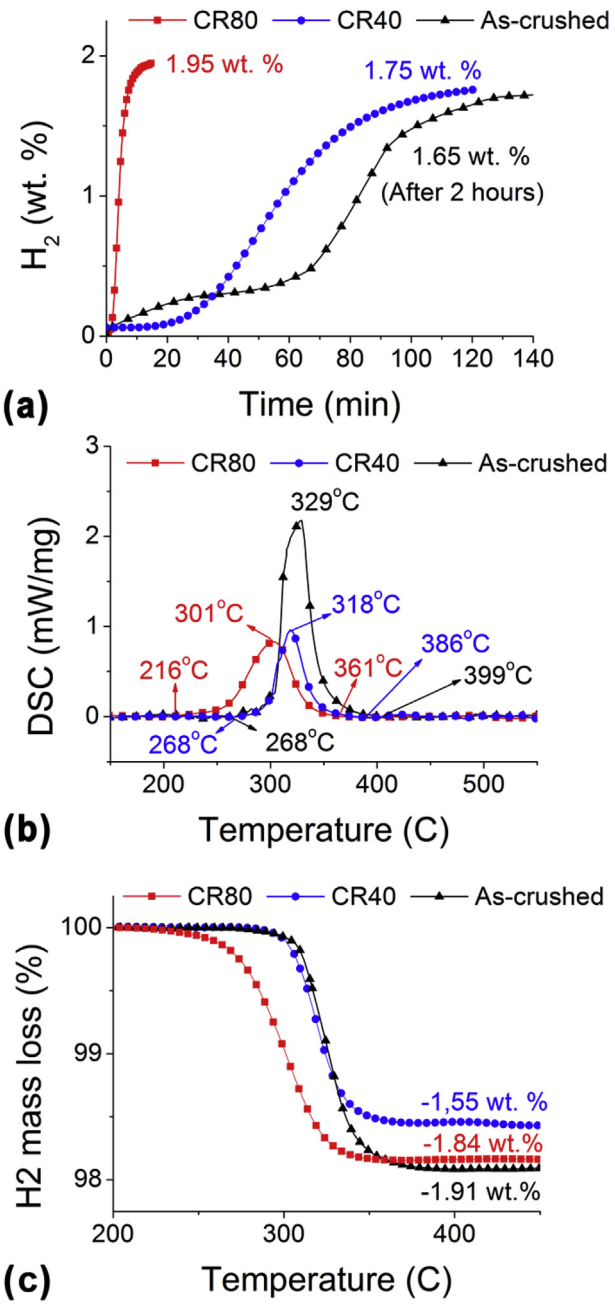

Fig. 6 – (a) Hydrogen absorption kinetics at 300 °C for as-crushed and cold rolled samples, (b) DSC analysis, (c) TGA desorption properties of the hydrogenated samples.

Table 3 – Results of volumetric measurements (Sievert's method) for samples as-crushed, CR40, and CR80.

Sample	Sievert's-type apparatus			
	Absorption			
	Time (h)	Temperature (°C)	H_2 Pressure (MPa)	H_2 (wt.%)
As-crushed	15	300	2	2.14
	2			1.65
CR40	2	RT		1.75
CR80	0.25			1.95

the sample CR40, except for some foils on the surface, the middle of the sample is formed by a ~25 μm thick layer, thus hampering fast hydrogen diffusion into the whole bulk. The worst condition is for the as-crushed sample, in whose volume, even after hydrogenation at 300 °C, there is the absence of any residual porosity (interlayer in the case of samples CR40 and CR80), consequently, not creating an easily accessible path for hydrogen penetration into the thick bulk of about 1 mm^3. Additionally to the effect of thickness, the kinetics could have a synergetic effect of crystallite size and sample deformation (Table 3), by increasing the surface area and density of defects, respectively, as the deformation increases.

As can be observed in Table 3, the capacities for samples processed by ECR are lower than for the as-crushed one. The presence of the α"-Ti phase (Fig. 4) could be one reason for this. However, the amounts of α" in the ECR samples are very similar, thus not justifying the difference between them. In this case, it must be born in mind that the hydrogenation of the as-crushed sample was thermally assisted, while in the other two cases, it was at the room temperature. Also, in the case of sample CR40, one can observe that it did not reach its maximum capacity. This fact is apparent since its respective absorption curve would continue growing with a slow rate to achieve a steady-state as it happened with the as-crushed sample that took 15 h to reach its maximum capacity assisted by the high absorption temperature.

Furthermore, regarding capacities, it is imperative to emphasize the importance of the processing route, sample morphology, and the conditions of the sample surface (for instance, cracks). By comparing our previous results for powders of the same alloy [52], it is possible to see that the sample CR80 reached almost the same capacity as powders hydrogenated at 100 °C. Indeed, the kinetics in the case of those powders was much faster than in the case of sample CR80 in the initial stage of the hydrogenation because of the much higher surface area and higher absorption temperature.

Other few results can be found in the literature for comparison. Table 4 presents comparative results between ECR samples of this work and samples with similar characteristics found in the literature. Despite the different variables used in each work, some conclusions can be drawn from the comparison. For example, the H-absorption times to reach half of the theoretical H-storage capacity of β-Ti alloys (1.44 wt% H_2) can be used to contrast the results. As one may observe, despite the higher pressure, which was applied to hydrogenate sample $Ti_{0.67}Nb_{0.33}$ [37], our sample CR80 produced results kinetically similar undoubtedly due to the particular microstructure and morphology with particle size (surface) of about 3 mm stacked with very thin layers full of defects (crystalline defects (dislocations, grain/subgrain boundaries), cracks, and stored strain energy).

Fig. 6b and c present DSC analysis and thermogravimetric desorption properties of the hydrogenated samples, respectively. In this case, please refer to Table 5, which resumes desorption temperatures values obtained from DSC analysis and desorption capacities obtained from TGA data. Considering absorption at RT, from those plots, it is clear that the amount of desorbed hydrogen also increases with the increase of CR passes. Evidently, the as-crushed sample desorbed a bit more just because it absorbed more. As evidenced in our previous work [52], desorbed capacities were smaller than the absorbed ones. The tendency of desorption verified for all mechanically processed samples of the studied alloy is per the literature [33]. As suggested before [53], desorption capacities of Ti–Nb alloys decrease due to the hydrogen entrapping inside octahedral sites that can impair desorption capacities and the reversibility of such alloys [47,53,74–78].

It is also to be noted the decrease in the starting desorption temperature (Fig. 6b and c and Table 5) of sample CR80, which evidences the importance of the morphology of the samples and, again, the influence of thin layers. More evident is the peak temperature for desorption, which clearly decreases

Table 4 – Comparative results between ECR samples of this work and similar samples reported in the literature. H-absorption times to reach half of the theoretical H-storage capacity of β-Ti alloys (1.44 wt % H_2).

Sample	Sievert's-type apparatus (Absorption)				Ref.
	Activation	Temperature (°C)	H_2 Pressure (MPa)	Time (min)	
CR40	Mechanical	RT	2	76.4	This work
CR80	Mechanical	RT	2	4.93	
$Ti_{0.67}Nb_{0.33}$ alloy[a]	Thermal	RT	2.5	<1	[37]
BCC Ti–Al–Nb alloys[a]	Thermal	500	1.2	6.92	[36]

[a] Alloys are in the form of powders.

Table 5 – Results regarding desorption temperatures values and desorption capacities obtained by calorimetry (thermal analysis) for the samples as-crushed, CR40, and CR80.

Sample	Absorption Time (h)	Thermal Analysis after the first absorption		
		DSC analysis		TGA
		Desorption Temperatures		
		Onset (°C)	Peak (°C)	(wt. %)
As-crushed	15	268	329	−1.91
CR40	2	268	318	−1.15
CR80	0.25	216	301	−1.84

with the amount of deformation. It is interesting to note that desorption temperatures are smaller than observed for powder samples of the same composition reported in our previous work [52], highlighting again the importance of the processing route, the quality of the surface, assured by cold rolling under protective atmosphere, and the sample morphology.

Summary and conclusions

Refined β Ti–40Nb alloy, to be used as hydrogen storage material, was produced by a combined route of rapid solidification and extensive cold rolling (ECR) under a controlled inert atmosphere. ECR of the crushed quenched alloy resulted in two kinds of stacking layers; thicker ones for 40 CR passes and thinner for 80 CR passes. Both types of samples had high densities of crystalline defects, cracks, microstrains, and clean surfaces. After analyzing results and related discussions, it was possible to reach the following conclusions:

- ✓ ECR of β Ti–40Nb alloy performed under inert atmosphere resulted in very fast hydrogen sorption properties at room temperature without any previous thermal activation procedure.
- ✓ High densities of crystalline defects (dislocations, grain/subgrain boundaries, cracks, microstrains, and clean surfaces had a significant effect in improving the kinetic behavior for hydrogen absorption at low temperature. Such an improvement was also correlated to the synergetic effect of the above-resulting features after deformation and thickness of stacked layers in the different deformation conditions.
- ✓ At room temperature, samples deformed with 80 passes acquired better kinetics and absorbed 1.95 wt% of H_2 in 15 min, while 1.75 wt% was the amount absorbed after 2 h by samples deformed with 40 passes.
- ✓ The worst sorption kinetics was presented by undeformed samples that were hydrogenated at 300 °C and acquired a capacity of 1.65 wt% after 2 h. Such a result is related to the absence of defects and the large thickness of the samples.
- ✓ The hydrogen desorption evolved in the same way as for absorption regarding deformation, which also influenced desorption temperatures that increased from ~220 °C, for specimens rolled with 80 passes to ~270 °C for samples deformed with 40 passes and samples undeformed.
- ✓ No significant loss in hydrogen capacity was observed in the cold rolled samples, despite the formation of the α" phase, which does not contribute to the formation of TiNb hydride.

Acknowledgments

The authors acknowledge the financial support provided by the São Paulo Research Foundation FAPESP (grant number 2013/05987-8). The Structural Characterization Laboratory (LCE) at the Federal University of São Carlos for the microscopy and x-ray facilities. The authors gratefully acknowledge the financial support of National Council for Scientific and Technological Development (CNPq). AMJJ would like to acknowledge the CNPq under grant #301429/2017-0.

Appendix A. Supplementary data

Supplementary data to this article can be found online at https://doi.org/10.1016/j.ijhydene.2019.05.211.

REFERENCES

[1] Tao K, Arano H, Zhang P, Ai P, Han L, Tsubaki N. Enhanced hydrogen production from steam reforming of vegetable oil over bimodal ZrO_2-SiO_2 supported Ni catalyst. Chem Select 2017;2:527–32.
[2] Hosseini SE, Wahid MA. Hydrogen production from renewable and sustainable energy resources: promising green energy carrier for clean development. Renew Sustain Energy Rev 2016;57:850–66.
[3] Kapdan IK, Kargi F. Bio-hydrogen production from waste materials. Enzym Microb Technol 2006;38:569–82.
[4] Wang Y, Deng W, Liu X, Wang X. Electrochemical hydrogen storage properties of ball milled multi-wall carbon nanotubes. Int J Hydrogen Energy 2009;43:1437–43.
[5] Ni M, Leung DYC, Leung MKH. A review on reforming bio-ethanol for hydrogen production. Int J Hydrogen Energy 2007;32:3238–47.
[6] Ozarslan A. Large-scale hydrogen energy storage in salt caverns. Int J Hydrogen Energy 2012;37:14265–77.
[7] Züttel A, Remhof A, Borgschulte A, Friedrichs O. Hydrogen: the future energy carrier. Phil Trans R Soc A 2010;368:3329–34.
[8] Li S, Pan W, Mao Z. A comparative study of the electrochemical hydrogen storage properties of activated carbon and well-aligned carbon nanotubes mixed with copper. Int J Hydrogen Energy 2005;30:643–8.
[9] Lueking AS, Pan L, Narayanan DL. Effect of expanded graphite lattice in exfoliated graphite nanofibers on hydrogen storage. J Phys Chem B 2005;109:12710–7.
[10] Zeng K, Zhang D. Recent progress in alkaline water electrolysis for hydrogen production and applications, Energy Combust. Science 2010;36:307–26.
[11] Mishra A, Banerjee S, Mohapatra SK, Graeve QA, Misr M. Synthesis of carbon nanotube–TiO_2 nanotubular material for reversible hydrogen storage. Nanotechnology 2008;19:445607–14.
[12] Fang B, Zhou H, Honma I. Ordered porous carbon with tailored pore size for electrochemical hydrogen storage application. J Phys Chem B 2006;110:4875–80.
[13] Strobel R, Garche J, Moseley PT, Jorissen L. Hydrogen storage by carbon materials. J Power Sources 2006;159:781–801.
[14] Frackowiak E, Beguin F. Electrochemical storage of energy in carbon nanotubes and nanostructured carbons. Carbon 2002;40:1775–87.
[15] Varin RA, Czujko T, Wronski ZS. Nanomaterials for solid state hydrogen storage. New York: Springer; 2009.
[16] Sakintuna B, Lamari-Darkrim F, Hirscher M. Metal hydride materials for solid hydrogen storage. Int J Hydrogen Energy 2007;32(9):1121–40.
[17] Li J, Wang H, Liu J, Ruan J. Effects of Nb addition on microstructure and mechanical properties of TiNiNb alloys fabricated by elemental powder sintering. Mater Sci Eng A 2014;609:235–40.

[18] Sharma B, Vajpai S, Ameyama K. Microstructure and properties of beta Ti-Nb alloy prepared by powder metallurgy route using titanium hydride powder. J Alloy Comp 2016;656:978–86.
[19] Kent D, Wang G, Dargusch M. Effects of phase stability and processing on the mechanical properties of Ti–Nb based β Ti alloys. J Mech Behav Biomed Mater 2013;28:15–25.
[20] Zhuravleva K, Bönisch M, Scudino S, Calin M, Schultz L, Eckert J, et al. Phase transformations in ball-milled Ti–40Nb and Ti–45Nb powders upon quenching from the ß-phase region. Powder Technol 2014;253:166–71.
[21] Lindemann I, Schmidt R, Pilz S, Gebel B, Teresiak A, Gebert A. Ultrafine-grained Ti-40Nb prepared by reactive milling of the elements in hydrogen. J Alloy Comp 2017;729:1244–9.
[22] Chen Z, Liu Y, Jiang H, Liu M, Wang CH, Cao GH. Microstructures and mechanical properties of Mn modified, Ti-Nb-based alloys. J Alloy Comp 2017;723:1091–7.
[23] Wang Q, Han C, Choma T, Wei Q, Yan C, Song B, et al. Effect of Nb content on microstructure, property and in vitro apatite-forming capability of Ti-Nb alloys fabricated via selective laser melting. Mater Des 2017;126:268–77.
[24] Bahador A, Hamzah E, Kondoh K, Bakar TAA, Yusof F, Imai H, et al. Effect of deformation on the microstructure, transformation temperature and superelasticity of Ti–23 at% Nb shape-memory alloys. Mater Des 2017;118:152–62.
[25] Sun B, Meng XL, Gao ZY, Cai W, Zhao LC. Effect of annealing temperature on shape memory effect of cold-rolled Ti-16 at.%Nb alloy. J Alloy Comp 2017;715:16–20.
[26] Gui Y-w, Oh J-M, Lim J-W. Sintering properties of Ti-27Nb alloys prepared by using Ti/TiH2 powders under argon and hydrogen sintering processes. Powder Technol 2018;339:775–80.
[27] Karre R, Kodli BK, Rajendran A, Nivedhitha J, Pattanayak DK, Ameyama K, et al. Comparative study on Ti-Nb binary alloys fabricated through spark plasma sintering and conventional P/M routes for biomedical application. Mater Sci Eng C 2019;94:619–27.
[28] Maghsoudlou A, Zarei-Hanzaki A, Abedi HR, Barabi A, Pilehva F, Dietrich D, et al. The room temperature tensile deformation behavior of thermomechanically processed β-metastable Ti-Nb-Ta-Zr bio-alloy: the role of deformation-induced martensite. Mater Sci Eng A 2018;738:15–23.
[29] Tobe H, Kim HY, Inamura T, Hosoda H, Nam TH, Miyazaki S. Effect of Nb content on deformation behavior and shape memory properties of Ti–Nb alloys. J Alloy Comp 2013;577(1):S435–8.
[30] Sun B, Meng XL, Gao ZY, Cai W. Martensite structure and mechanical property of Ti-Nb-Ag shape memory alloys for biomedical applications. Vacuum 2018;156:181–6.
[31] Wang P, Todai M, Nakano T. ω-phase transformation and lattice modulation in biomedical β-phase Ti-Nb-Al alloys. J Alloy Comp 2018;766:511–6.
[32] Ma T, Chen R, Zheng D, Guo J, Ding H, Su Y, et al. Effect of β-phase stabilizing elements and high temperature (1373–1693 K) on hydrogen absorption in TiAl alloys. Int J Hydrogen Energy 2017;42:86–95.
[33] Aleksanyan AG, Dolukhanyan SK, Shekhtman VS, Khasanov SS, Ter-Galstyan OP, Martirosyan MV. Formation of alloys in the Ti-Nb system by hydride cycle method and synthesis of their hydrides in self-propagating high-temperature synthesis. Int J Hydrogen Energy 2012;37:14234–9.
[34] Huot J. Enhancing hydrogen storage properties of metal hybrides: enhancement by mechanical deformations. Springer; 2016. p. 30.
[35] Wang X-l, Zhao Y-q, Wei X-w, Hou H-l. Microstructures of TC21 alloys after hydrogenation and dehydrogenation. Trans Nonferrous Metals Soc China 2014;24:82–8.
[36] Patselov AM, Rybin VV, Greenberg BA, Mushnikov NV. Hydrogen absorption in as-cast bcc single-phase Ti–Al–Nb alloys. J Alloy Comp 2010;505:183–7.
[37] Ruz P, Kumar A, Banerjee S, Meena SS, Pillai CGS. Hydrogen absorption characteristics and Mössbauer spectroscopic study of $Ti_{0.67}Nb_{0.33}$–xFe_x (x=0.00, 0.13, 0.20) alloys. J Alloy Comp 2014;585:120–8.
[38] Yuan B-g, Zheng Y-b, Wang Y-j, Gong L-q. Hydrogen absorption characteristics and microstructural evolution of TC21 titanium alloy. Trans Nonferrous Metals Soc China 2016;26:599–606.
[39] Zhang LT, Ito K, Vasudevan VK, Yamaguchi M. Beneficial effects of O-phase on the hydrogen absorption of Ti–Al–Nb alloys. Intermetallics 2001;9(12):1045–52.
[40] Ito K, Zhang LT, Vasudevan VK, Yamaguchi M. Multiphase and microstructure effects on the hydrogen absorption/desorption behavior of a Ti–22Al–27Nb alloy. Acta Mater 200;49(6):963-972.
[41] Sun P, Fang ZZ, Koopman M, Paramore J, Ravi Chandran KS, Ren Y, et al. An experimental study of the (Ti–6Al–4V)–xH phase diagram using in situ synchrotron XRD and TGA/DSC techniques. Acta Mater 2015;84:29–41. 2015.
[42] Popov AA, Illarionov AG, Demakov SL, Elkina OA. Study of phase transformations in the titanium-niobium-hydrogen system. Int J Hydrogen Energy 1997;22:195–200.
[43] Yan E, Li X, Rettenmayr M, Liu D, Su Y, Guo J, et al. Design of hydrogen permeable Nb–Ni–Ti alloys by correlating the microstructures, solidification paths and hydrogen permeability. Int J Hydrogen Energy 2014;39:3505–16.
[44] Luo W, Ishikawa K, Aoki K. Highly hydrogen permeable Nb–Ti–Co hypereutectic alloys containing much primary bcc-(Nb, Ti) phase. Int J Hydrogen Energy 2012;37:12793–7.
[45] Magnone E, Jeon SI, Park JH, Fleury E. Relationship between microstructure and hydrogen permeation properties in the multiphase Ni21Ti23Nb56 alloy membranes. J Membr Sci 2011;384:136–41.
[46] Yexin C. Kinetics of hydrogen diffusion in Ti-6Al-4V alloy. Rare Metal Mater Eng 2015;44:553–6.
[47] Keller T, Rettenmayr M. Hydrogen diffusion in Ti–Nb45 at high hydrogen contents. J Alloy Comp 2007;437:180–5.
[48] Ilyin AA, Kollerov MYu, Golovin IS. Hydrogen influence on plastic deformation mechanism of β-titanium alloys of Ti–Nb system. J Alloy Comp 1997;253–254:144–7.
[49] Okamoto H. Nb-Ti (Niobium-Titanium). J Phase Equilibria 2002;23:553.
[50] Pathak A, Banumathy S, Sankarasubramanian R, Singh AK. Orthorhombic martensitic phase in Ti–Nb alloys: a first principles study. Comput Mater Sci 2014;83:222–8.
[51] Zhang Y, Liu H, Jin Z. Thermodynamic assessment of the Nb-Ti system. Calphad 2001;25:305–17.
[52] de Araujo-Silva R, Neves AM, Vega LER, Triques MRM, Leiva DR, Kiminami CS, et al. Synthesis of β-Ti-Nb alloys from elemental powders by high-energy ball milling and their hydrogenation features. Int J Hydrogen Energy 2018;43:18382–91.
[53] Klebanoff L. Hydrogen storage technology: materials and applications. Boca Raton: Taylor & Franc; 2013.
[54] Maziarz W, Lejkowska M, Michalski A, Dutkiewicz J. Transmission electron microscopy studies of microstructure of Ti–Nb and Ti–Ta alloys after ball milling and hot consolidation. J Microsc 2006;224:42–5.
[55] Fischer M, Joguet D, Robin G, Peltier L, Laheurte P. In situ elaboration of a binary Ti–26Nb alloy by selective laser melting of elemental titanium and niobium mixed powders. Mater Sci Eng C 2016;62:852–9.
[56] Ouyang LZ, Cao ZJ, Wang H, Liu JW, Sun DL, Zhang QA, et al. Enhanced dehydriding thermodynamics and kinetics in Mg(In)–MgF_2 composite directly synthesized by plasma milling. J Alloy Comp 2014;586:113–7.

[57] Ouyang LZ, Ye SY, Dong HW, Zhua M. Effect of interfacial free energy on hydriding reaction of Mg–Ni thin films. Appl Phys Lett 2007;90:2.
[58] Ouyang LZ, Cao ZJ, Li LL, Wang H, Liu JW, Min D, et al. Enhanced high-rate discharge properties of La11.3Mg6.0Sm7.4Ni61.0Co7.2Al7.1 with added graphene synthesized by plasma milling. Int J Hydrogen Energy 2014;39(24):12765–72.
[59] Ouyang LZ, Cao ZJ, Wang H, Liu JW, Sun DL, Zhang QA, et al. Dual-tuning effect of in on the thermodynamic and kinetic properties of Mg2Ni dehydrogenation. Int J Hydrogen Energy 2013;38(21):8881–7.
[60] Cao Z, Ouyang L, Wu Y, Wang H, Liu J, Fang F, et al. Dual-tuning effects of In, Al, and Ti on the thermodynamics and kinetics of Mg85In5Al5Ti5 alloy synthesized by plasma milling. J Alloy Comp 2015;623:354–8.
[61] Ouyang LZ, Yang XS, Zhu M, Liu JW, Dong HW, Sun DL, et al. Enhanced hydrogen storage kinetics and stability by synergistic effects of in situ formed $CeH_{2.73}$ and Ni in $CeH_{2.73}$-MgH_2-Ni nanocomposites. J Phys Chem C 2014;118(15):7808–20.
[62] Zhu M, Wang H, Ouyang LZ, Zeng MQ. Composite structure and hydrogen storage properties in Mg-base alloys. Int J Hydrogen Energy 2006;31(2):251–7.
[63] Kashkarov EB, Nikitenkov NN, Sutygina AN, Obrosov A, Manakhov A, Polčák J, et al. Hydrogen absorption by Ti-implanted Zr-1Nb alloy. Int J Hydrogen Energy 2018;43:2484–91.
[64] Fallah V, Amoorezaei M, Provatas N, Corbin SF, Khajepour A. Phase-field simulation of solidification morphology in laser powder deposition of Ti–Nb alloys. Acta Mater 2012;60:1633–46.
[65] Lutterotti L, Ceccato R, DalMaschio R, Pagani E. Mater Sci Forum 1998;87:278–81.
[66] Lutterotti L, MAUD - Materials Analysis Using Diffraction, http://maud.radiographema.eu/, accessed: Feb 2019.
[67] Jorge Jr AM, Prokofiev E, de Lima GF, Rauch E, Veron M, Botta WJ, et al. An investigation of hydrogen storage in a magnesium-based alloy processed by equal-channel angular pressing. Int J Hydrogen Energy 2013;38:8306–12.
[68] Jorge Jr AM, de Lima GF, Triques MRM, Botta WJ, Kiminami CS, Nogueira RP, et al. Correlation between hydrogen storage properties and textures induced in magnesium through ECAP and cold rolling. Int J Hydrogen Energy 2014;39:3810–21.
[69] de Lima GF, Peres MM, Garroni S, Baró MD, Surinyach S, Kiminami CS, et al. Microstructural characterization and hydrogenation study of extruded MgFe alloy. J Alloy Comp 2010;504:S299–301.
[70] de Lima GF, Garroni S, Baró MD, Suriñach S, Kiminami CS, Botta WJ, et al. 2Mg–Fe alloys processed by hot-extrusion: influence of processing temperature and the presence of MgO and MgH_2 on hydrogenation sorption properties. J Alloy Comp 2011;509:S460–3.
[71] Guo Y, Georgarakis K, Yokoyama Y, Yavari AR. On the mechanical properties of TiNb based alloys. J Alloy Comp 2013;571:25–30.
[72] Terayama A, Fuyama N, Yamashita Y, Ishizaki I, Kyogoku H. Fabrication of Ti–Nb alloys by powder metallurgy process and their shape memory characteristics. J Alloy Comp 2013;577:S408–12.
[73] Stadelmann P. [Internet]. Java-ems: JEMS. 2004. Available from: http://cimewww.epfl.ch/people/stadelmann/jemsWebSite/jems.html.
[74] Hsu Y-S, Perng T-P. Hydrogenation of multicomponent Zr-base C15 type alloys. J Alloy Comp 1995;227(2):180–5.
[75] Lototskyy MV, Yartys VA, Pollet BG, Bowman Jr RC. Metal hydride hydrogen compressor: a review. Int J Hydrogen Energy 2014;39:5818–51.
[76] Silverstein R, Eliezer D, Tal-Gutelmacher E. Hydrogen trapping in alloys studied by thermal desorption spectrometry. J Alloy Comp 2018;747:511–22.
[77] Wang Y-B, Northwood DO. Calculations of the enthalpy of metal hydride formation. J Less Common Met 1987;135:239–45.
[78] Kashkarov EB, Nikitenkov NN, Sutygina AN, Bezmaternykh AO, Kudiiarov VN, Syrtanov MS, et al. Hydrogenation behavior of Ti-implanted Zr-1Nb alloy with TiN films deposited using filtered vacuum arc and magnetron sputtering. Appl Surf Sci 2018;432:207–13.